Applied Catalysis B: Environmental 331 (2023) 122687

Contents lists available at ScienceDirect

Applied Catalysis B: Environmental

journal homepage: www.elsevier.com/locate/apcatb

N, O trans-coordinating silver single-atom catalyst for robust and efficient ammonia electrosynthesis from nitrate

Zhen Shen [a,b], Yingsong Yu [c], Zhiwei Zhao [c], Muhammad Asim Mushtaq [a], Qianqian Ji [a], Ghulam Yasin [a], Lashari Najeeb Ur Rehman [a], Xiaochun Liu [e,f], Xingke Cai [a], Panagiotis Tsiakaras [d], Jie Zhao [a,*]

[a] Institute for Advanced Studies (IAS), Shenzhen University, Shenzhen 518060, China
[b] School of Chemistry and Chemical Engineering, Nanjing University, Nanjing 210023, China
[c] College of Textile Science and Engineering (International institute of Silk), Zhejiang Sci-Tech University, Hangzhou 310018, China
[d] Laboratory of Alternative Energy Conversion Systems Department of Mechanical Engineering School of Engineering, University of Thessaly, 1 Sekeri Str., Pedion Areos 38834, Greece
[e] Institute of Metals, College of Material Science and Engineering, Changsha University of Science & Technology, Changsha 410004, China
[f] Shenzhen Focalon Applied Academy, Shenzhen Practical Scientific Research Co., Ltd, Shenzhen 518132, China

ARTICLE INFO

Keywords:
Silver
Single-atom catalyst
Ammonia electrosynthesis
Nitrate
Plasma-driven nitrogen oxidation

ABSTRACT

Single-atom catalysts (SACs) containing noble metals have been largely explored for various catalytic reactions and demonstrated high activity and chemical stability but are rarely used for electrocatalytic nitrate reduction to ammonia (NO_3^-RA) because of their strong tendency towards hydrogen evolution reaction (HER). Herein, we developed the N, O trans-coordination strategy to inhibit the HER of carbon nanotube-based Ag SACs (Ag_1/NOCNT) catalyst, thus improving the NH_3 production. The Ag_1/NOCNT exhibits a record-high ammonia yield rate (YR_{NH3}) of 90 mol h^{-1} g_{Ag}^{-1}, more than two folds of the best-reported SACs using carbon supports, as well as high Faradaic efficiency (FE_{NH3}) of 97.9% and optimal electrochemical stability. These excellent performances attribute to the novel trans AgN_2O_2 configuration, suppressing the HER, optimizing the adsorption of intermediates and facilitating the potential-determining step in NO_3^-RA. The corresponding plasma-driven nitrogen oxidation and NO_x^- reduction coupling system presented high YR_{NH3} of ~1.3 mol h^{-1} g^{-1} (~41.5 mol h^{-1} g_{Ag}^{-1}) and FE_{NH3} of 85.2%, demonstrating high feasibility for sustainable green NH_3 synthesis over specially designed catalytic materials under ambient conditions.

1. Introduction

Electrocatalytic nitrate reduction to NH_3 (NO_3^-RA) is regarded as a promising alternative for the energy-intensive Haber-Bosch process, as it can be driven by renewable electricity, using naturally available abundant water as the hydrogen donor and operate under ambient conditions [1,2]. Currently, NO_3^- as a pollutant in the water environment is usually removed by converting into N_2 gas through a complex denitrification process [3,4], while the electrocatalytic conversion of NO_3^- to NH_3 generates value-added NH_3 product as well as helps to overcome NO_3^- pollution [5–9]. Furthermore, plasma-driven N_2 oxidation (pNO) coupled with NO_3^-RA is a unique two steps strategy for green NH_3 synthesis, which has been recently thrust into the spotlight and fully driven by electric energy using water and air (or N_2 and O_2), as well as operates at ambient conditions [10–14]. In recent years, the NO_3^-RA has become the crucial reaction for NO_3^- removal and green NH_3 production.

The NO_3^-RA ($NO_3^- + 6\ H_2O + 8e^- \rightarrow NH_3 + 9OH^-$) is a complex reaction involving the transfer of nine protons and eight electrons, which includes multiple non-spontaneous hydrogenation reactions of $*NO_x$ (e.g., $*NO_3 \rightarrow *NO_3H$, $*NO_2 \rightarrow *NO_2H$, and $*NO \rightarrow *NOH$) [15–17]. Under the reduction potential of NO_3^-RA, the self-hydrogenation of adsorbed hydrogen (*H) generated from H_2O dissociation triggers the inevitable competitive hydrogen evolution reaction (HER), leading to a low selectivity of NH_3 product [18–21]. For traditional metal catalysts, a decent NH_3 selectivity is usually attainable at low overpotentials with small current densities, but corresponding to a low NH_3 yield rate [22,23]. In principle, a highly selective catalyst should facilitate the *H formation and increase the utilization of *H to

* Corresponding author.
E-mail addresses: zhaojie@szu.edu.cn, zhaojienju@163.com (J. Zhao).

https://doi.org/10.1016/j.apcatb.2023.122687
Received 16 January 2023; Received in revised form 18 March 2023; Accepted 22 March 2023
Available online 24 March 2023
0926-3373/

promote hydrogenation of $^*NO_x$ (i.e., $^*NO_3$, $^*NO_2$ and $^*NO$) thus enhancing NH_3 selectivity and yield while inhibiting the HER [24,25]. The incorporation of surface oxygen and heteroatoms on the metals have been reported to strengthen the $^*H$ adsorption and accelerate $^*H$ transfer for the hydrogenation reactions of $^*NO_x$, respectively [26–28]. These methods were usually implemented on the bulk- or nanoparticle-scale active metals with low utilization of metal atoms. Due to the multistep reaction pathways involving eight electron transfer processes, bulk- and nanoparticle-scale active metals with adjacent metal catalytic sites could easily lead to N−N coupling and the formation of dinitrogen by-products, e.g., N_2O, N_2 and N_2H_4, which cannot further ensure the reduction of nitrogenous species to NH_3 and decreases NH_3 selectivity [4,15,29,30].

Single-atom catalysts (SACs) present the maximal atom utilization due to the atomic dispersion of active metal species [31–35]. The isolated metal catalytic sites eradicate the N−N coupling [36]. Notably, the activity and selectivity of SACs are easily tunable by developing uniformly dispersed active metal centers and regulating their coordination structures [37–42]. Due to these unique advantages, SACs have attracted many research interests in NO_3^-RA, presenting unusual activity and selectivity [13, 19, 36–48]. Although noble metal SACs possess high activity and chemical stability, they suffer from the competitive HER during the work potential of NO_3^-RA [16]. To date, most studies carried out on NO_3^-RA were comprised of non-noble metal SACs, such as Cu, Fe, and Co but seldom on noble metal-based SACs [13, 19, 36–38, 43], especially on carbon supports with tunable heteroatoms as the coordination sites for metal centers [49,50]. Therefore, it is challenging to develop advanced noble metal-based SACs with both high catalytic activity and high NH_3 selectivity for high-yield NH_3 production.

Silver (Ag) has high chemical stability and the lowest-cost advantage over other noble metals. Herein, we used the N, O trans-coordination strategy to improve the NH_3 selectivity and yield of Ag SACs. Specifically, the N, O trans-coordinated Ag SACs (denoted as Ag_1/NOCNT) were constructed by using Ag^+ ions and the N, O co-doped carbon nanotubes (NOCNT) through a simple impregnation-annealing process. As a NO_3^-RA catalyst, Ag_1/NOCNT exhibits a record-high NH_3 yield rate (YR_{NH3}) of 90 mol h^{-1} g_{Ag}^{-1} (1530 g h^{-1} g_{Ag}^{-1}), more than two folds of the high-performance single-atom catalysts with carbon supports, as well as a high NH_3 Faradaic efficiency (FE_{NH3}) of 97.9% and good electrochemical stability. These excellent NO_3^-RA performances are attributed to the high atom utilization and unique trans AgN_2O_2 configuration for suppressing the competitive HER, optimizing the adsorption of intermediates and facilitating the potential-determining steps. The corresponding plasma-driven nitrogen oxidation and NO_x^- reduction (pNO–NO_x^-RA) coupled application system presents high FE_{NH3} of 85.2% and YR_{NH3} of ~1.3 mol h^{-1} g^{-1} (~41.5 mol h^{-1} g_{Ag}^{-1}; 705.5 g h^{-1} g_{Ag}^{-1}) with plasma time of 120 min, which demonstrates high feasibility for sustainable green NH_3 synthesis under ambient conditions.

2. Experimental section

2.1. Synthesis of the N, O co-doped carbon nanotubes

The N, O co-doped carbon nanotubes (NOCNT) was synthesized by in situ chemical vapor deposition at 650 °C with Fe-Co/γ-Al_2O_3 and pyridine as the catalyst and the carbon source, respectively [51,52]. The as-prepared NOCNT/Fe-Co/γ-Al_2O_3 were refluxed in 6 M NaOH at 90 °C and 6 M HCl at 110 °C for three times to remove the Fe-Co/γ-Al_2O_3 catalysts. Then the purified NOCNT was washed with distilled water several times until the pH of the filtrate reached 7, and then dried at 70 °C overnight.

2.2. Synthesis of the N, O trans-coordinated Ag SACs

The N, O trans-coordinated Ag SACs (i.e., Ag_1/NOCNT) was prepared by the impregnation-annealing method. 20 mg NOCNTs were ultrasonically dispersed in 50 mL of ultrapure water (18.2 MΩ·cm), and then 50 μL of 0.1 mol L^{-1} $AgNO_3$ solution was dropped into the dispersion with stirring, followed by the continuing stirring for 10 h. After that, the sample was filtered, freeze-dried, and then annealed in a furnace by supplying 50 sccm of Ar at 450 °C for 2 h, leading to the formation of Ag_1/NOCNT.

2.3. Synthesis of the Ag nanoparticles/NOCNT catalyst

For comparison, the Ag nanoparticles/NOCNT catalyst (i.e., Ag_{NP}/NOCNT) was synthesized by a microwave-assisted ethylene glycol (EG) reduction method. Typically, 20 mg of NOCNT was dispersed ultrasonically into 50 mL of EG, and then 100 μL of 0.5 mol L^{-1} $AgNO_3$/EG and 2 mL of 0.2 mol L^{-1} NaOH/EG solution were successively added to the suspension and this mixture was stirred for 4 h. The suspension was irradiated in a microwave oven at 700 W for 60 s followed by aging for 5 min. After that, the sample was filtered and washed with ethanol and ultrapure water, freeze-dried, and then annealed in a furnace by supplying 50 sccm of H_2/Ar at 450 °C for 2 h, leading to the formation of Ag_{NP}/NOCNT.

2.4. Electrochemical measurements

5.0 mg of catalysts (Ag_1/NOCNT, Ag_{NP}/NOCNT, or NOCNT) were dispersed ultrasonically into a mixed solution containing 0.8 mL of ultrapure water, 0.2 mL of ethanol, and 150 μL of 5 wt% Nafion solution, followed by stirring overnight. 3 μL of the catalyst ink was dropped onto the glassy carbon electrode (3 mm diameter) for natural drying at room temperature. The catalyst mass loading on the working electrode was 0.18 mg cm^{-2}. Ag/AgCl electrode (3 M KCl with a salt bridge) and platinum sheet (1 cm × 1 cm) were used as the reference and counter electrodes, respectively. 0.5 M Na_2SO_4 solution containing 50 mM $NaNO_3$ was used as the electrolyte. The pH was adjusted to 12 by 2 mol L^{-1} NaOH to provide an alkaline condition and avoid the decrease in H_2O and NO_3^- adsorption on catalyst surface by the competitive adsorption of excessive OH^- (e.g., pH>13).

The electrochemical measurements were conducted on a VMP3 electrochemical workstation (Biologic). The NO_3^-RA experiments were performed using a three-electrode system in a 10 mL H-type electrolytic cell separated by a pretreated proton-exchange membrane (Nafion 117). All potentials were converted to the reversible hydrogen electrode (RHE) potential by the following formula: $E_{RHE} = E_{Ag/AgCl} + 0.059 \times pH + 0.209$ V. 20 sccm of Ar gas flowed through the cathodic compartment for 20 min before each electrochemical test and continuously supply during NO_3^-RA experiment. The linear sweep voltammetry (LSV) tests were performed at a scan rate of 10 mV s^{-1}. The chronoamperometric tests were conducted at different potentials for 0.5 h with a rotation rate of 300 rpm, and the cyclic stability tests were conducted for 0.5 h per cycle. The absorption solution of 0.05 M H_2SO_4 was used to collect the evaporated NH_3 in tail gas from the cathodic compartment. The cathodic and anodic compartment electrolytes and the absorption solution were used to calculate the NH_3 yield rate and Faradaic efficiency.

The amount of catalytic site is reflected in the electrochemical active surface area (ECSA), which is proportional to the electrochemical double layer capacitance (C_{dl}). C_{dl} was determined by cyclic voltammetry curves at different scan rates of 50, 100, 150, 200, and 250 mV s^{-1} in a non-Faradaic potential window. The plot of current density against the scan rate has a linear relationship and the slope is equivalent to C_{dl}. The double-layer capacitance of Ag referred to polished Cu foil is 29 μF cm^{-2} [53,54]. Thus, the ECSA of the catalyst can be calculated as ECSA = C_{dl}/(29 μF cm^{-2} per cm^2_{ECSA}).

3. Results and discussion

3.1. Synthesis and characterizations of Ag_1/NOCNT

Single Ag atoms loaded on the N, O co-doped carbon nanotubes (Ag_1/NOCNT) were fabricated by a simple impregnation-annealing method. Ag species were anchored on N/O sites on NOCNT support through the strong metal-support interactions (Fig. 1a). For comparison, the Ag nanoparticle on NOCNT (Ag_{NP}/NOCNT) was prepared by a microwave-assisted ethylene glycol reduction method. The X-ray powder diffraction (XRD) pattern of Ag_1/NOCNT shows no obvious peaks assigned to crystalline Ag, implying no aggregates of Ag were formed, indicating the uniform dispersion of Ag single atoms over NOCNT substrate (Fig. 1b). The scanning electron microscopy (SEM) and the low-resolution transmission electron microscopy (TEM) images of Ag_1/NOCNT exhibit typical nanotube morphology with high length–diameter ratio and hollow structure (Fig. 1c), similar to the NOCNT support (Fig. S1). This hollow structure corresponding to the pore size of 10 nm endows a large specific surface area of 190 m^2 g^{-1}, close to the NOCNT support (194 m^2 g^{-1}) (Fig. 1c and Fig. S2). The lattice fringes of 0.34 nm are assigned to the (002) facet of graphite-2H in the high-resolution transmission electron microscopy (HR-TEM) image of Ag_1/NOCNT (Fig. 1d). No particles can be observed on NOCNT (Fig. 1c-d). The atomic-resolution high-angle annular dark-field scanning transmission electron microscopy (HAADF-STEM) image of Ag_1/NOCNT clearly displays that the isolated Ag atoms (bright spots) randomly disperse on the NOCNT support (Fig. 1e). These Ag atoms, along with the N and O atoms, were detected uniformly distributing on NOCNT by energy dispersive X-ray spectroscopy (EDS) elemental mappings (Fig. 1f and Fig. S3). Ag nanoparticles with 20–50 nm are observed in Ag_{NP}/NOCNT (Fig. S4). The mass loading of Ag in Ag_1/NOCNT and Ag_{NP}/NOCNT is 3.13 wt% and 32.20 wt%, respectively, determined by inductively coupled plasma-optical emission spectroscopy (ICP-OES) analysis. A negligible fluctuation of I_D/I_G value from Raman spectra of Ag_1/NOCNT, Ag_{NP}/NOCNT and NOCNT indicates the structural stability of NOCNT support (Fig. S5).

The chemical and atomic structure of the Ag_1/NOCNT were further investigated by X-ray photoelectron spectroscopy (XPS) and X-ray absorption spectroscopy (XAS). NOCNT support has a high content of N and O dopants, providing abundant active sites for anchoring Ag atoms (Fig. S6). The Ag 3d XPS spectra of both Ag_1/NOCNT and Ag_{NP}/NOCNT present two peaks at 368.5 and 374.5 eV, which belong to the Ag $3d_{5/2}$ and Ag $3d_{3/2}$, respectively (Fig. 2a). No obvious shifts of the peaks are observed between Ag_1/NOCNT and Ag_{NP}/NOCNT. The binding energy

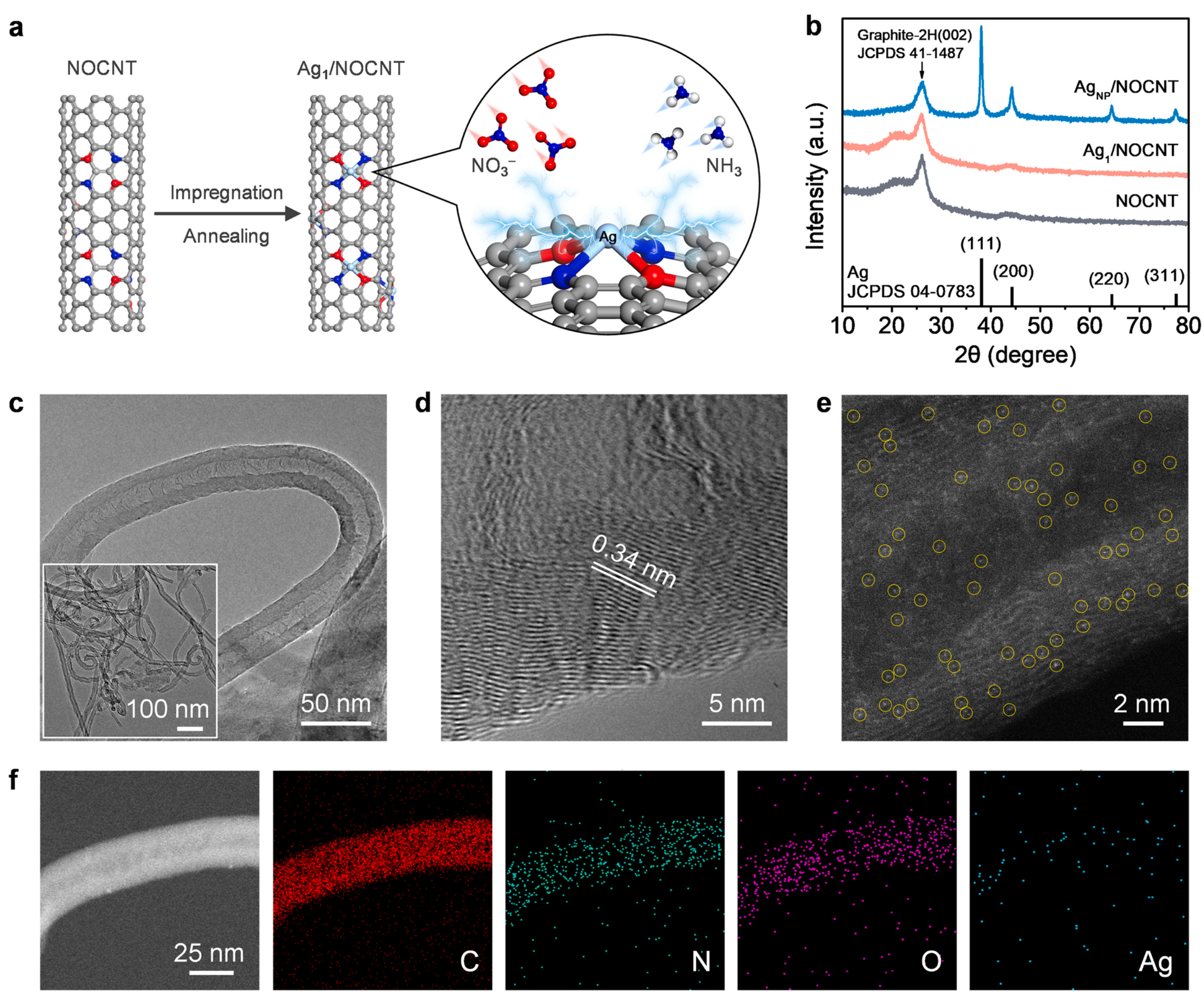

Fig. 1. Synthesis and morphology characterization of Ag_1/NOCNT. (a) Schematic synthesis. (b) XRD patterns. (c) TEM images. (d) HR-TEM image. (e) Atomic-resolution HAADF-STEM image. The Ag single atoms were circled. (f) STEM image and EDS element mappings.

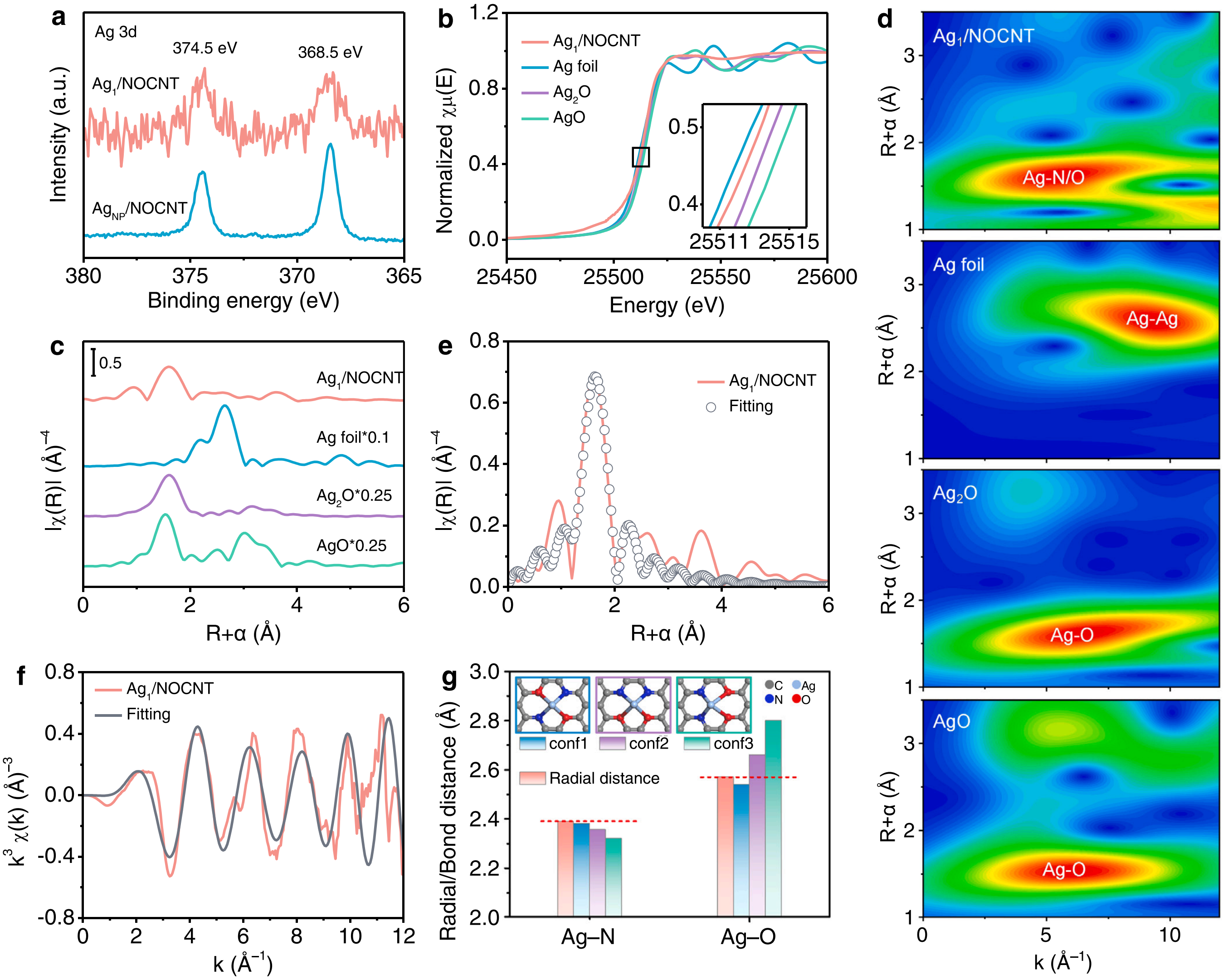

Fig. 2. Structural analysis of Ag_1/NOCNT. (a) Ag 3d XPS spectra. (b) Ag K-edge XANES spectra. (c) Ag K-edge FT-EXAFS spectra. (d) WT of the Ag K-edge FT-EXAFS spectra. (e, f) Fitting results of the EXAFS spectra of Ag_1/NOCNT at R space (e) and k-space (f). (g) Determination of the coordination structure by comparing of EXAFS fitting results and theoretical model data. Inset: three possible configurations.

difference of 6 eV corresponds to Ag^0 [55]. The Ag K-edge X-ray absorption near-edge structure (XANES) of Ag_1/NOCNT shows near-edge absorption energy between Ag metal foil and Ag_2O references (Fig. 2b). The XPS and XANES results indicate the oxidation state of Ag atoms is between Ag^0 and Ag^+ and close to Ag^0. The Fourier transformed k^3-weighted extended X-ray absorption fine structure (FT-EXAFS) spectrum of Ag_1/NOCNT exhibits a dominant peak at 1.62 Å from Ag–N or Ag–O path, along with the absence of a peak at 2.64 Å from Ag–Ag path (Fig. 2c). The wavelet transforms (WT) plot of Ag K-edge FT-EXAFS oscillation for Ag_1/NOCNT displays only one intensity maximum at ~5.5 $Å^{-1}$, which is assigned to the Ag–N or Ag–O contribution (Fig. 2d). No other intensity maximum belonging to Ag–Ag contribution (~9.31 $Å^{-1}$) in the WT plot of Ag_1/NOCNT, compared with that of Ag foil. These results verify that the Ag atoms with Ag–N or Ag–O coordination are atomically dispersed in the NOCNT support, and no Ag clusters or nanoparticles exist. The combination of FT-EXAFS fitting and a theoretical model was used to determine the coordination configuration of the Ag single atoms. The fitting results for the first coordination shell indicate that the Ag atom is coordinated with two N atoms and two O atoms (Fig. 2e, f and Table S1). Three possible coordination configurations of AgN_2O_2 and the corresponding bond distances between Ag atom and N or O atoms were proposed and optimized by density functional theory (DFT) calculation (Fig. S7). As shown in Fig. 2g, the radial distances of Ag–N/O obtained from FT-EXAFS fitting are well matched with the bond lengths of Ag–N/O in the trans configuration (i. e., conf1 shown in the inset). These results indicate that the Ag atom is coordinated with two N atoms and two O atoms with a trans configuration.

3.2. Electrocatalytic nitrate reduction to ammonia performance

NO_3^-RA was performed in a three-electrode system in H-type cell. The linear sweep voltammetry (LSV) curves of Ag_1/NOCNT, Ag_{NP}/NOCNT, and NOCNT show that the onset potentials positive shift in the electrolyte with NO_3^- compared with those without NO_3^-, along with larger current densities (j) (Fig. 3a), which are attributed to the domination of NO_3^-RA in the competition with HER. The lower Tafel slope renders Ag_1/NOCNT presenting the larger catalytic j at high overpotential, thus the j of Ag_1/NOCNT could surpass that of Ag_{NP}/NOCNT (Fig. S8). The NO_3^-RA performances of the catalysts were investigated by chronoamperometry test at −0.3 to −0.7 V for 30 min (Fig. S9). The possible liquid products, including NH_3, NO_2^-, and N_2H_4, were quantified by ultraviolet-visible (UV–Vis) spectrophotometry (Fig. S10), while the gaseous products like N_2 and H_2 were quantified using gas

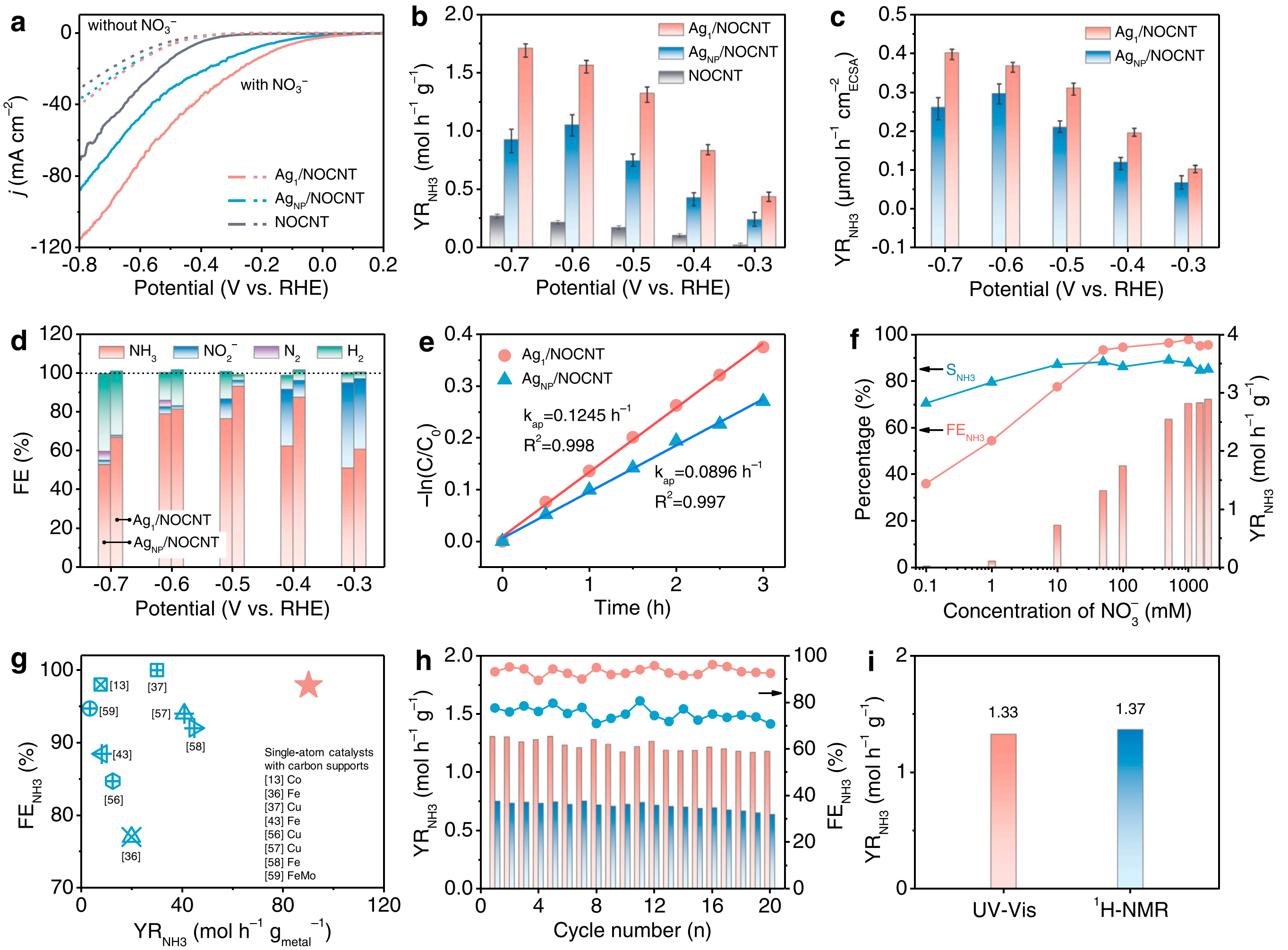

Fig. 3. NO_3^-RA performance. (a) LSV curves obtained with the electrolyte with and without NO_3^-. (b-d) YR_{NH3} (b), YR_{NH3} normalized by ECSA (c), and FE of the products (d) at different applied potentials in 50 mM NO_3^-. (e) Kinetic profiles at −0.5 V with initial NO_3^- concentrations of 10 mM. (f) YR_{NH3}, FE_{NH3}, and S_{NH3} at −0.5 V for 0.5 h with different NO_3^- concentrations. (g) Comparison of NO_3^-RA performance of Ag_1/NOCNT with reported single-site catalysts with carbon supports. (h) Electrochemical durability of Ag_1/NOCNT and Ag_{NP}/NOCNT at −0.5 V in 50 mM NO_3^-. (i) YR_{NH3} quantified by UV-Vis and ^{1}H NMR.

chromatography. At all applied potentials, the YR_{NH3} of Ag_1/NOCNT (1.33 mol h^{-1} g^{-1} or 42.5 mol h^{-1} g_{Ag}^{-1} at −0.5 V) is higher than that of Ag_{NP}/NOCNT and much greater than that of NOCNT, indicating the NO_3^-RA activity of Ag_1/NOCNT mainly originates from Ag (Fig. 3b and Fig. S11). The larger electrochemical active surface area (ECSA) of Ag_1/NOCNT than that of Ag_{NP}/NOCNT indicates more catalytic sites on Ag_1/NOCNT profited by the atomic dispersion of Ag (Fig. S12). When normalized by ECSA, the YR_{NH3} of Ag_1/NOCNT is higher than that of Ag_{NP}/NOCNT, suggesting the higher reactivity of the trans AgN_2O_2 site of Ag_1/NOCNT than that of the Ag−Ag site of Ag_{NP}/NOCNT (Fig. 3c). The turnover frequency (TOF) of Ag_1/NOCNT is calculated to be 1.4 s^{-1}, 2.3 times higher than that of Ag_{NP}/NOCNT (0.6 s^{-1}), indicating the higher intrinsic activity for the former. The FE of products (NH_3, NO_2^-, N_2, and H_2) of Ag_1/NOCNT and Ag_{NP}/NOCNT are listed in Fig. 3d (Fig. S13). Both FE_{NH3} deliver 'volcano curves' at the potential range of −0.3 to −0.7 V. And the FE_{NH3} of Ag_1/NOCNT reaches the maximum of 93.4% at −0.5 V whereas for Ag_{NP}/NOCNT is 79.0% at −0.6 V. The degressive FE_{NH3} at the lower and higher potentials are mainly attributed to the enhanced NO_3^--to-NO_2^- and HER, respectively. No N_2 was detected at all applied potentials for Ag_1/NOCNT, while it was produced at high potentials of −0.6 V and −0.7 V for Ag_{NP}/NOCNT, confirming the eradication for N_2 formation by the isolate catalytic sites in a single-atom catalyst. Ag_1/NOCNT also exhibits high selectivity of NH_3 (S_{NH3}) and NH_3 partial current density at all applied potentials, superior to Ag_{NP}/NOCNT (Fig. S14). The conversion rates of NO_3^- (C_{NO3-}) were calculated from the evolution of NO_3^- concentration over NO_3^-RA time. The C_{NO3-} of Ag_1/NOCNT are higher than those of Ag_{NP}/NOCNT in all periods and reaches 84% after 3 h (Fig. S15).

To evaluate the advantages of the N,O coordination and the atomic Ag, we measured the NO_3^-RA performances of Ag SACs on N-doped carbon nanotubes (Ag_1/NCNT) and O-doped carbon nanotubes (Ag_1/OCNT), Ag nanoparticles on carbon nanotubes (Ag_{NP}/CNT) and bulk Ag (Ag sheet). As shown in Fig. S16, Ag_1/NOCNT presents the higher YR_{NH3} (or YR_{NH3} normalized to Ag) and FE_{NH3} than Ag_1/NCNT and Ag_1/OCNT at all potentials, indicating the improved NO_3^-RA performance is attributed to the synergism of N,O coordination. Additionally, Ag_1/NOCNT also shows much higher NO_3^-RA performances than Ag_{NP}/CNT and Ag sheet, confirming the atomically dispersed Ag is of superior activity to the nanoscale and bulk Ag (Fig. S17). These results indicate that the synergistic effect of N,O-coordination and atomic Ag in Ag_1/NOCNT leads to the excellent NO_3^-RA performance.

The NO_3^-RA on the basis of the time-dependent concentration changes of NO_3^- obeys first-order kinetics (Fig. 3e and Fig. S18), suggesting that even in an electrolyte with high NO_3^- concentration, the reaction rate of the catalyst is sufficiently fast and only limited by NO_3^- diffusion [37]. Ag_1/NOCNT shows a larger apparent rate constant (k) than Ag/NOCNT, indicating the faster reaction rate of the former. The S_{NH3} of Ag_1/NOCNT show high levels > 70% at different NO_3^-

concentrations from 0.1 mM to 2000 mM, indicating the excellent adaptability of Ag_1/NOCNT for NO_3^- concentrations (Fig. 3f and Fig. S19). This makes Ag_1/NOCNT available for various NO_3^-RA applications with different NO_3^- concentrations, such as natural water treatment with low NO_3^- concentrations to NH_3 synthesis with high NO_3^- concentrations. The YR_{NH3} and FE_{NH3} reach 2.8 mol h^{-1} g^{-1} and 97.9%, respectively, at the NO_3^- concentrations of 1000 mM. When normalized by the mass loading of Ag, the YR_{NH3} achieves 90 mol h^{-1} g_{Ag}^{-1} (1530 g h^{-1} g_{Ag}^{-1}), which is more than two folds of the best-reported single-atom catalysts with carbon supports (Fig. 3g) [13, 36, 37, 43, 56–59]. The FE_{NH3}, S_{NH3} and C_{NO3-} at the optimal potential reach high levels (Table S2).

Ag_1/NOCNT exhibit a weak fluctuation in FE_{NH3} and an extremely slight decay in YR_{NH3} during the NO_3^-RA test upto twenty cycles, as well as the atomically dispersed Ag in the support after long cycles, indicating good electrochemical stability (Fig. 3h, Figs. S20 and S21). Ag_{NP}/NOCNT also show good stability with weak fluctuation in FE_{NH3} and slight decay in YR_{NH3}. A long-time NO_3^-RA with large amount of electrolyte (500 mL) was performed in a flow cell (Fig. S22). During five-hour NO_3^-RA, both Ag_1/NOCNT and Ag_{NP}/NOCNT deliver stable *i–t* curves, confirming their excellent stability. Ag_1/NOCNT exhibits larger current density, higher YR_{NH3} and FE_{NH3} than Ag_{NP}/NOCNT. This long-time NO_3^-RA with large amount of electrolyte demonstrates the potential application in NO_3^- control and NH_3 recycling.

To exclude the possible interference of N-presence in catalysts, electrolytes and experimental setup, the blank test and ^{15}N isotope labeling experiments were conducted. Ag_1/NOCNT show ignorable YR_{NH3} in absence of NO_3^- containing electrolyte compared with NO_3^- at −0.5 V (Fig. S23). $^{15}NO_3^-$ and $^{14}NO_3^-$ (i.e., NO_3^- in all NO_3^-RA in this study) were respectively used as the nitrogen source for NO_3^-RA, and the electrolytes after NO_3^-RA were detected by ^1H nuclear magnetic resonance (^1H NMR). The ^1H NMR spectrum of the electrolyte with $^{15}NO_3^-$ displays a couple-peak assigned to $^{15}NH_4^+$, while that of the electrolyte with $^{14}NO_3^-$ shows a triple-peak assigned to $^{14}NH_4^+$ (Fig. S24). The integral area ratios of the peaks of NH_4^+ to that of dimethyl sulfoxide (DMSO) show similar values. These confirm that the NH_3 in the electrolyte was all obtained from the NO_3^- conversion. NMR test was also employed for verifying the accuracy of UV-Vis results. The standard curve of the given $^{15}NH_4^+$ concentrations versus the integral area of $^{15}NH_4^+$ peaks in the ^1H NMR spectra was obtained (Fig. S25). When using $Na^{15}NO_3$ as the N-source in NO_3^-RA, Ag_1/NOCNT exhibits similar YR_{NH3} quantified by ^1H NMR to that by UV-Vis, proving the accuracy of quantitative methods.

3.3. DFT calculations

The intrinsic mechanism for the excellent NO_3^-RA performance of Ag_1/NOCNT is investigated by density functional theory (DFT) calculations. On the basis of the characterization results, we constructed a trans configuration of AgN_2O_2 in graphene for Ag_1/NOCNT, as well as Ag(111), Ag(200), Ag(220) and Ag(311) for Ag_{NP}/NOCNT (Fig. S26). Projected partial density of state (PDOS) analysis reveals an upshifting *d*-band center of trans AgN_2O_2 (−3.74 eV vs. Femi level) compared with those of the four Ag facets, i.e., Ag(111), Ag(200), Ag(220) and Ag(311) (−4.16, −4.37, −4.06, and −4.18 eV vs. Femi level, respectively) (Fig. 4a), suggesting the enhanced adsorption of the reactants/reactive intermediates on trans AgN_2O_2. In NO_3^-RA, hydrogen is obtained from H_2O dissociation and promptly consume during NO_3^-RA, thus inhibiting the competitive HER. Accordingly, the catalysts should have a strong

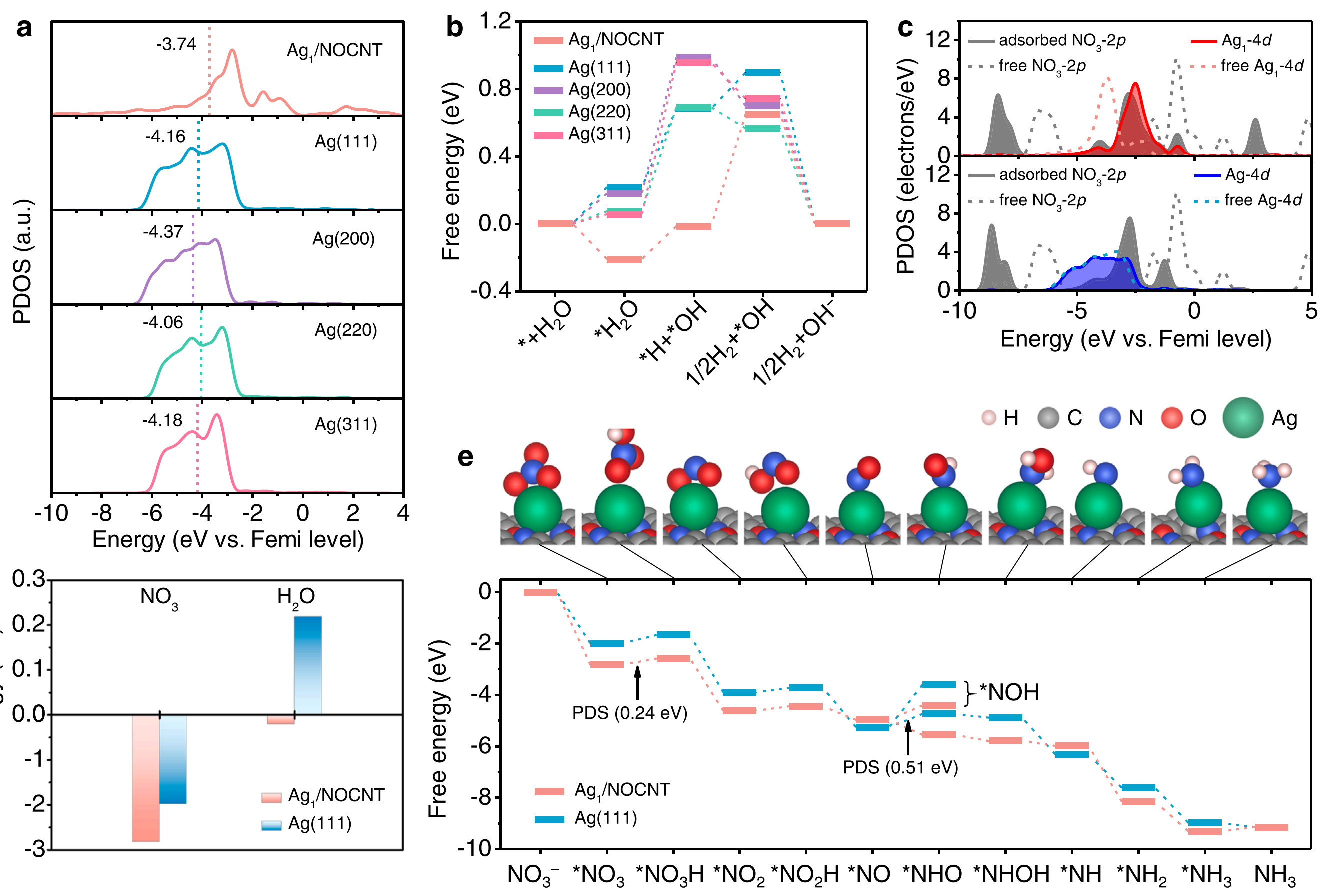

Fig. 4. DFT calculations. (a) Projected densities of state (PDOS) for *d* band center calculation. (b) Gibbs free-energy diagram of water dissociation. (c) PDOS for free NO_3 and NO_3 adsorbed on Ag site in trans AgN_2O_2 (top) and Ag(111) (bottom). (d) Adsorption energies of NO_3 and H_2O on trans AgN_2O_2 and Ag(111). (e) Gibbs free-energy diagram of NO_3^-RA and the corresponding adsorption configuration of intermediate for Ag_1/NOCNT.

H_2O adsorption and dissociation capacity to facilitate the Volmer step, meanwhile a strong *H adsorption to suppress Heyrovsky step [43]. Trans AgN_2O_2 exhibits exothermal adsorption of H_2O because of the upshifting *d*-band center, while the four facets of Ag undergo endothermal processes (Fig. 4b). The trans AgN_2O_2 shows the much smaller and larger Gibbs free-energy differences (ΔG) respectively in the dissociation of $^*H_2O$ and the desorption of *H than the four facets of Ag and the two cis AgN_2O_2 (Fig. S27). These results indicate that the Ag_1/NOCNT with trans AgN_2O_2 configuration facilitates the dissociation of H_2O and inhibits the desorption of *H, thus promoting the supply of hydrogen for NH_3 formation and suppressing the competitive HER.

For NO_3^- reduction, the initial steps, including the chemical adsorption of NO_3^- and the deoxygenation from $^*NO_3$ to $^*NO_2$, are regarded as the rate-limiting step [16]. The interaction between NO_3 and the catalysts is disclosed by PDOS analysis for NO_3 adsorption (Fig. 4c). Once NO_3^- ions are adsorbed, the 2*p* orbitals of $^*NO_3$ downshift and the 4*d* orbitals of the corresponding Ag shift upwards, supporting the electron transfer from the Ag site. The greater orbital overlap between them on trans AgN_2O_2 than on Ag(111) indicates the stronger interaction for the former, thus ensuring the more stable adsorption of $^*NO_3$ for the further reduction reaction. Such strong interaction leads to a more negative ΔG of $^*NO_3$ adsorption than the $^*H_2O$ adsorption, indicating the domination of the former in the competitive reaction environment (Fig. 4d). The Gibbs free-energy diagrams with optimized thermodynamic elementary steps in NO_3^-RA are shown in Fig. 4e and Fig. S28. The adsorption of NO_3^- and the formation of $^*NO_2$ for trans AgN_2O_2 show more negative ΔG than those of the four Ag facets (Fig. S29). Owing to the enhanced adsorption capacity of trans AgN_2O_2 by the upshifting *d*-band center, the hydrogenations of $^*NO_3$ (i.e., $^*NO_3 \rightarrow {}^*NO_3H$) and $^*NO_2$ (i.e., $^*NO_2 \rightarrow {}^*NO_2H$), respectively, are also facilitated. The subsequent reaction pathway from *NO leads to the formation of NH_3 and N_2. In the NH_3 generation pathways on both trans AgN_2O_2 and Ag(111), the hydrogenations at the N-atom on *NO are easier than O-atom. The formation of *NHO on Ag(111) presents a large ΔG of 0.51 eV, which is the potential-determining step (PDS) of NO_3^-RA. Notably, this step on trans AgN_2O_2 is exothermal, i.e., $\Delta G = -0.58$ eV, leading to the shift of the PDS to the formation of $^*NO_3H$ with a much lower ΔG of 0.24 eV. Such ΔG of PDS for the trans configuration is also lower than those for the two cis configurations, indicating the promotion of trans configuration for the hydrogenation of $^*NO_3$ to $^*NO_3H$ (Fig. S30). The NO, N_2O, and N_2 pathways on both trans AgN_2O_2 and Ag (111) are proved unfavorable compared with NH_3 pathways (Fig. S31). The ΔG of the $^*NO \rightarrow {}^*N_2O_2$ pathway on Ag(111) is close to that of the $^*NO \rightarrow {}^*NHO$ pathway, unveiling the activity origin for N_2 production on Ag_{NP}/NOCNT. These confirm that the excellent NO_3^-RA performance of Ag_1/NOCNT with trans AgN_2O_2 configuration is attributed to the promotion of hydrogen supply, the enhanced adsorption of NO_3^- and the decreased activation energy barrier of PDS.

3.4. Coupled pNO–NO_x^-RA system for sustainable green NH_3 synthesis

The practical application of Ag_1/NOCNT catalyst for NH_3 synthesis is demonstrated by a coupled plasma-driven N_2 oxidation with nitrogen oxyanion reduction (pNO–NO_x^-RA) system. The schematic illustration is shown in Fig. 5a. Standard air was used as the reactant that was triggered by a plasma generator driven by dielectric barrier discharge and converted into nitrogen oxyanions (NO_x) (Fig. S32). The mixture of air and NO_x was then bubbled into the electrolyte, during which the NO_x was converted into NO_x^- (NO_2^- and NO_3^-) [60]. By pNO for 120 min, the total concentration of NO_x^- in the electrolyte reached 18 mM (Fig. 5b). Later, the electrolyte was used for the electrosynthesis of NH_3, where water served as a hydrogen donor. The obtained LSV curves of

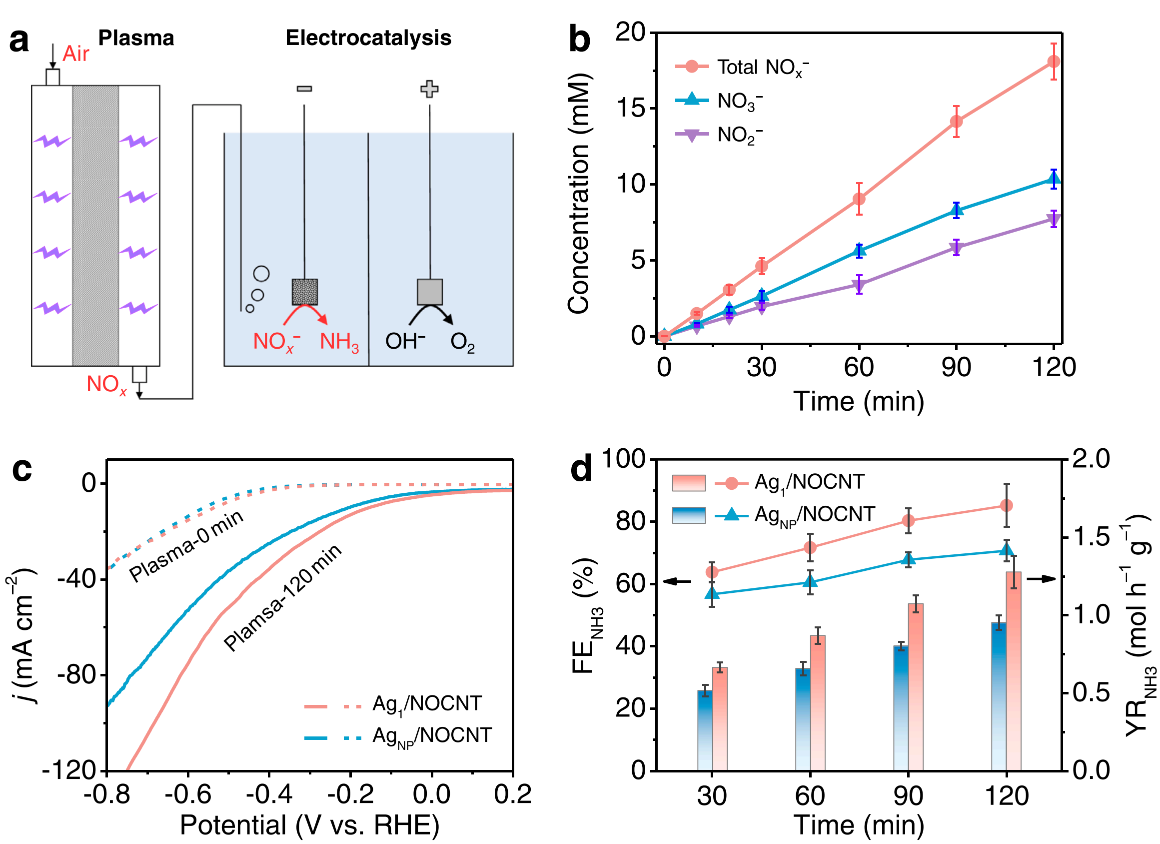

Fig. 5. Coupled pNO–NO_x^-RA for sustainable NH_3 synthesis. (a) Schematic illustration of the coupled reaction system. (b) Plots of NO_x^- concentration vs. plasma operation time. (c) LSV curves of Ag_1/NOCNT and Ag_{NP}/NOCNT in NO_3^-RA without and with plasma operation time for 120 min (d) NO_3^-RA performances of Ag_1/NOCNT and Ag_{NP}/NOCNT at − 0.5 V in coupled pNO–NO_x^-RA with different plasma operation times.

Ag_1/NOCNT and Ag_{NP}/NOCNT deliver more positive onset potential and much larger current density than that in the case without plasma treatment (Fig. 5c). NO_x^-RA performances of the two catalysts with different plasma treatment intervals were conducted at −0.5 V for 30 min (Fig. S33). With prolonging the plasma treatment time, both Ag_1/NOCNT and Ag/NOCNT show incremental FE_{NH3} and YR_{NH3} due to the increase of NO_x^- concentration (Fig. 5d). And Ag_1/NOCNT outperforms Ag_{NP}/NOCNT in all plasma treatment times. Significantly, Ag_1/NOCNT exhibits high FE_{NH3} of 85.2% and YR_{NH3} of ~1.3 mol h^{-1} g^{-1} (~41.5 mol h^{-1} g_{Ag}^{-1}; 705.5 g h^{-1} g_{Ag}^{-1}) with plasma time of 120 min, superior to the most reported catalysts with the electrolyte prepared with the end-product of $NaNO_3$ or KNO_3 (Fig. 3g). Predictably, NO_x^- will be produced in large scale by increasing the plasma efficiency and the NH_3 synthesis can be significantly enhanced (Fig. 3f). The blank experiment results show a trace of NO_x^- generated by air bubbling without plasma treatment and negligible NH_3 generated during electrocatalysis (Fig. S34). These results indicate that the NH_3 synthesized from NO_x^-RA purely originated from air and water.

Practical applications of NO_x^-RA, such as pilot scaling of NO_x^-RA from industrial wastewater [61], and solar-power-/friction-power-driven NO_x^-RA [62,63] have been developed. These demonstrations were only conducted in specific scenarios with the condition that NO_x^- was directly used as the nitrogen source. Notably, our coupled pNO–NO_x^-RA system is not limited by regions and scenarios because the nitrogen and hydrogen sources are globally available in the form of air and water, respectively, and the only driving force is electricity. Predictably, once the electricity price reduces to a certain level with the further development and utilization of renewable energy, the coupled pNO–NO_x^-RA system will become a promising alternative for commercial NH_3 synthesis.

4. Conclusion

In summary, we developed the trans N,O-coordination strategy to improve the NH_3 selectivity and yield of noble metal-based SACs. Specifically, with relatively low-cost Ag as the research object, the trans N, O-coordinated Ag SACs (denoted as Ag_1/NOCNT) were constructed by Ag^+ ions and the N, O co-doped carbon nanotubes (NOCNT) via a facile impregnation-annealing process. HAADF-STEM and XAS analysis verify that the atomically dispersed Ag is anchored on NOCNT in a unique trans AgN_2O_2 configuration. Due to such isolated catalytic sites, N_2 formation is completely eradicated on Ag_1/NOCNT. The Ag_1/NOCNT catalyst exhibits a record-high NH_3 yield rate of 90 mol h^{-1} g_{Ag}^{-1} (1530 g h^{-1} g_{Ag}^{-1}), more than two folds of the best-reported SACs using carbon supports, as well as a good NH_3 selectivity of 94.3% (at −0.7 V), high NH_3 Faradaic efficiency of 97.9%, excellent adaptability for NO_3^- concentrations and good electrochemical stability. The blank experiment and ^{15}N isotope labeling NMR test verify the accuracy of NH_3 quantification. Experimental and theoretical results reveal that the excellent NO_3^-RA performance of Ag_1/NOCNT is attributed to the novel trans AgN_2O_2 configuration for suppressing the competitive HER, optimizing the adsorption of intermediates, and facilitating the potential-determining step. In a coupled pNO-NO_x^-RA system, Ag_1/NOCNT catalyst presents outstanding activity and selectivity for NH_3 production, demonstrating its promising applications for sustainable and distributed NH_3 synthesis under ambient conditions.

CRediT authorship contribution statement

Zhen Shen: Conceptualization, Methodology, Investigation, Data curation, Analysis, Writing – original draft, Writing – review & editing. **Yingsong Yu:** Investigation. **Zhiwei Zhao:** Investigation. **Muhammad Asim Mushtaq:** Investigation. **Qianqian Ji:** Investigation. **Ghulam Yasin:** Investigation. **Lashari Najeeb Ur Rehman:** Investigation. **Xiaochun Liu:** Investigation. **Xingke Cai:** Investigation. **Panagiotis Tsiakaras:** Investigation. **Jie Zhao:** Conceptualization, Methodology, Investigation, Writing – review & editing.

Declaration of Competing Interest

The authors declare that they have no known competing financial interests or personal relationships that could have appeared to influence the work reported in this paper.

Data availability

Data will be made available on request.

Acknowledgements

This work was financially supported by Program B for Outstanding Ph.D. Candidate of Nanjing University (No. 202002B076). The authors thank the support and help of Prof. Zheng Hu's group (Nanjing University, China) for this work. The authors thank the Shanghai Synchrotron Radiation Facility (Shanghai, China) for the XAFS characterization.

Appendix A. Supporting information

Supplementary data associated with this article can be found in the online version at doi:10.1016/j.apcatb.2023.122687.

References

[1] Y. Wang, C. Wang, M. Li, Y. Yu, B. Zhang, Nitrate electroreduction: mechanism insight, in situ characterization, performance evaluation, and challenges, Chem. Soc. Rev. 50 (2021) 6720–6733.
[2] P.H. Van Langevelde, I. Katsounaros, M.T.M. Koper, Electrocatalytic nitrate reduction for sustainable ammonia production, Joule 5 (2021) 290–294.
[3] N. Lehnert, H.T. Dong, J.B. Harland, A.P. Hunt, C.J. White, Reversing nitrogen fixation, Nat. Rev. Chem. 2 (2018) 278–289.
[4] H. Xu, Y. Ma, J. Chen, W.X. Zhang, J. Yang, Electrocatalytic reduction of nitrate– a step towards a sustainable nitrogen cycle, Chem. Soc. Rev. 51 (2022) 2710–2758.
[5] W. He, J. Zhang, S. Dieckhofer, S. Varhade, A.C. Brix, A. Lielpetere, S. Seisel, J.R. C. Junqueira, W. Schuhmann, Splicing the active phases of copper/cobalt-based catalysts achieves high-rate tandem electroreduction of nitrate to ammonia, Nat. Commun. 13 (2022) 1129.
[6] Q. Gao, H.S. Pillai, Y. Huang, S. Liu, Q. Mu, X. Han, Z. Yan, H. Zhou, Q. He, H. Xin, H. Zhu, Breaking adsorption-energy scaling limitations of electrocatalytic nitrate reduction on intermetallic CuPd nanocubes by machine-learned insights, Nat. Commun. 13 (2022) 2338.
[7] W.X. Qiu, X.J. Chen, Y.T. Liu, D. Xiao, P.F. Wang, R. Li, K. Liu, Z.Y. Jin, P.P. Li, Confining intermediates within a catalytic nanoreactor facilitates nitrate-to-ammonia electrosynthesis, Appl. Catal. B Environ. 315 (2022), 121548.
[8] Y.L. Zhao, Y. Liu, Z.J. Zhang, Z.K. Mo, C.Y. Wang, S.Y. Gao, Flower-like open-structured polycrystalline copper with synergistic multi-crystal plane for efficient electrocatalytic reduction of nitrate to ammonia, Nano Energy 97 (2022), 107124.
[9] Z.J. Zhang, Y. Liu, X.Z. Su, Z.W. Zhao, Z.K. Mo, C.Y. Wang, Y.L. Zhao, Y. Chen, S. Y. Gao, Electro-triggered Joule heating method to synthesize single-phase CuNi nano-alloy catalyst for efficient electrocatalytic nitrate reduction toward ammonia, Nano Res. (2023), https://doi.org/10.1007/s12274-023-5402-y.
[10] Y. Ren, C. Yu, L. Wang, X. Tan, Z. Wang, Q. Wei, Y. Zhang, J. Qiu, Microscopic-level insights into the mechanism of enhanced NH_3 synthesis in plasma-enabled cascade N_2 oxidation–electroreduction system, J. Am. Chem. Soc. 144 (2022) 10193–10200.
[11] J. Sun, D. Alam, R. Daiyan, H. Masood, T.Q. Zhang, R.W. Zhou, P.J. Cullen, E. C. Lovell, A. Jalili, R. Amal, A hybrid plasma electrocatalytic process for sustainable ammonia production, Energy Environ. Sci. 14 (2021) 865–872.
[12] L. Li, C. Tang, X. Cui, Y. Zheng, X. Wang, H. Xu, S. Zhang, T. Shao, K. Davey, S. Z. Qiao, Efficient nitrogen fixation to ammonia through integration of plasma oxidation with electrocatalytic reduction, Angew. Chem. Int. Ed. 60 (2021) 14131–14137.
[13] A.J. Wu, J. Yang, B. Xu, X.Y. Wu, Y.H. Wang, X.J. Lv, Y.C. Ma, A.N. Xu, J.G. Zheng, Q.H. Tan, Y.Q. Peng, Z.F. Qi, H.F. Qi, J.F. Li, Y.L. Wang, J. Harding, X. Tu, A. Q. Wang, J.H. Yan, X.D. Li, Direct ammonia synthesis from the air via gliding arc plasma integrated with single atom electrocatalysis, Appl. Catal. B Environ. 299 (2021), 120667.
[14] Z. Meng, J.X. Yao, C.N. Sun, X. Kang, R. Gao, H.R. Li, B. Bi, Y.F. Zhu, J.M. Yan, Q. Jiang, Efficient ammonia production beginning from enhanced air activation, Adv. Energy Mater. 12 (2022), 2202105.
[15] M. Duca, M.T.M. Koper, Powering denitrification: the perspectives of electrocatalytic nitrate reduction, Energy Environ. Sci. 5 (2012) 9726–9742.

[16] S. Garcia-Segura, M. Lanzarini-Lopes, K. Hristovski, P. Westerhoff, Electrocatalytic reduction of nitrate: fundamentals to full-scale water treatment applications, Appl. Catal. B-Environ. 236 (2018) 546–568.
[17] Z. Shen, Y. Yu, Z. Zhao, S. Zhang, S. Xu, S. Yang, Y. Hu, Highly distributed amorphous copper catalyst for efficient ammonia electrosynthesis from nitrate, J. Hazard. Mater. 445 (2023), 130651.
[18] F.Y. Chen, Z.Y. Wu, S. Gupta, D.J. Rivera, S.V. Lambeets, S. Pecaut, J.Y.T. Kim, P. Zhu, Y.Z. Finfrock, D.M. Meira, G. King, G. Gao, W. Xu, D.A. Cullen, H. Zhou, Y. Han, D.E. Perea, C.L. Muhich, H. Wang, Efficient conversion of low-concentration nitrate sources into ammonia on a Ru-dispersed Cu nanowire electrocatalyst, Nat. Nanotechnol. 17 (2022) 759–767.
[19] G.F. Chen, Y.F. Yuan, H.F. Jiang, S.Y. Ren, L.X. Ding, L. Ma, T.P. Wu, J. Lu, H. H. Wang, Electrochemical reduction of nitrate to ammonia via direct eight-electron transfer using a copper–molecular solid catalyst, Nat. Energy 5 (2020) 605–613.
[20] M.A. Mushtaq, M. Arif, X. Fang, G. Yasin, W. Ye, M. Basharat, B. Zhou, S. Yang, S. Ji, D. Yan, Photoelectrochemical reduction of N_2 to NH_3 under ambient conditions through hierarchical $MoSe_2$@g-C_3N_4 heterojunctions, J. Mater. Chem. A 9 (2021) 2742–2753.
[21] M.A. Mushtaq, A. Kumar, G. Yasin, M. Arif, M. Tabish, S. Ibraheem, X.K. Cai, W. Ye, X.Y. Fang, A.L. Saad, J. Zhao, S.F. Ji, D.P. Yan, 3D interconnected porous Mo-doped WO_3@CdS hierarchical hollow heterostructures for efficient photoelectrochemical nitrogen reduction to ammonia, Appl. Catal. B Environ. 317 (2022), 121711.
[22] J.X. Liu, D. Richards, N. Singh, B.R. Goldsmith, Activity and selectivity trends in electrocatalytic nitrate reduction on transition metals, ACS Catal. 9 (2019) 7052–7064.
[23] I. Katsounaros, M.C. Figueiredo, X. Chen, F. Calle-Vallejo, M.T.M. Koper, Interconversions of nitrogen-containing species on Pt(100) and Pt(111) electrodes in acidic solutions containing nitrate, Electrochim. Acta 271 (2018) 77–83.
[24] Y.W. Ren, C. Yu, X.Y. Tan, H.L. Huang, Q.B. Wei, J.S. Qiu, Strategies to suppress hydrogen evolution for highly selective electrocatalytic nitrogen reduction: challenges and perspectives, Energy Environ. Sci. 14 (2021) 1176–1193.
[25] Y. Wang, H. Li, W. Zhou, X. Zhang, B. Zhang, Y. Yu, Structurally disordered RuO_2 nanosheets with rich oxygen vacancies for enhanced nitrate electroreduction to ammonia, Angew. Chem. Int. Ed. 61 (2022), e202202604.
[26] J. Li, G. Zhan, J. Yang, F. Quan, C. Mao, Y. Liu, B. Wang, F. Lei, L. Li, A.W.M. Chan, L. Xu, Y. Shi, Y. Du, W. Hao, P.K. Wong, J. Wang, S.X. Dou, L. Zhang, J.C. Yu, Efficient ammonia electrosynthesis from nitrate on strained ruthenium nanoclusters, J. Am. Chem. Soc. 142 (2020) 7036–7046.
[27] Q. Hu, Y.J. Qin, X.D. Wang, Z.Y. Wang, X.W. Huang, H.J. Zheng, K.R. Gao, H. P. Yang, P.X. Zhang, M.H. Shao, C.X. He, Reaction intermediate-mediated electrocatalyst synthesis favors specified facet and defect exposure for efficient nitrate–ammonia conversion, Energy Environ. Sci. 14 (2021) 4989–4997.
[28] Y. Wang, W. Zhou, R. Jia, Y. Yu, B. Zhang, Unveiling the activity origin of a copper-based electrocatalyst for selective nitrate reduction to ammonia, Angew. Chem. Int. Ed. 59 (2020) 5350–5354.
[29] A.C.A. De Vooys, G.L. Beltramo, B. Van Riet, J.A.R. Van Veen, M.T.M. Koper, Mechanisms of electrochemical reduction and oxidation of nitric oxide, Electrochim. Acta 49 (2004) 1307–1314.
[30] A.S. Dutton, J.M. Fukuto, K.N. Houk, Theoretical reduction potentials for nitrogen oxides from CBS-QB3 energetics and (c)PCM solvation calculations, Inorg. Chem. 44 (2005) 4024–4028.
[31] A.Q. Wang, J. Li, T. Zhang, Heterogeneous single-atom catalysis, Nat. Rev. Chem. 2 (2018) 65–81.
[32] S. Ji, Y. Chen, X. Wang, Z. Zhang, D. Wang, Y. Li, Chemical synthesis of single atomic site catalysts, Chem. Rev. 120 (2020) 11900–11955.
[33] S. Swain, A. Altaee, M. Saxena, A.K. Samal, A comprehensive study on heterogeneous single atom catalysis: current progress, and challenges, Coord. Chem. Rev. 470 (2022), 214710.
[34] S.K. Kaiser, Z. Chen, D. Faust Akl, S. Mitchell, J. Perez-Ramirez, Single-atom catalysts across the periodic table, Chem. Rev. 120 (2020) 11703–11809.
[35] W. Guo, Z. Wang, X. Wang, Y. Wu, General design concept for single-atom catalysts toward heterogeneous catalysis, Adv. Mater. 33 (2021), e2004287.
[36] Z.Y. Wu, M. Karamad, X. Yong, Q. Huang, D.A. Cullen, P. Zhu, C. Xia, Q. Xiao, M. Shakouri, F.Y. Chen, J.Y.T. Kim, Y. Xia, K. Heck, Y. Hu, M.S. Wong, Q. Li, I. Gates, S. Siahrostami, H. Wang, Electrochemical ammonia synthesis via nitrate reduction on Fe single atom catalyst, Nat. Commun. 12 (2021) 2870.
[37] X.F. Cheng, J.H. He, H.Q. Ji, H.Y. Zhang, Q. Cao, W.J. Sun, C.L. Yan, J.M. Lu, Coordination symmetry breaking of single-atom catalysts for robust and efficient nitrate electroreduction to ammonia, Adv. Mater. 34 (2022), e2205767.
[38] J. Li, M. Li, N. An, S. Zhang, Q. Song, Y. Yang, J. Li, X. Liu, Boosted ammonium production by single cobalt atom catalysts with high Faradic efficiencies, Proc. Natl. Acad. Sci. USA 119 (2022), E2123450119.
[39] D. Cao, H.X. Xu, H.L. Li, C. Feng, J. Zeng, D.J. Cheng, Volcano-type relationship between oxidation states and catalytic activity of single-atom catalysts towards hydrogen evolution, Nat. Commun. 13 (2022) 5843.
[40] D. Cao, Z.R. Zhang, Y.H. Cui, R.H. Zhang, L.P. Zhang, J. Zeng, D.J. Cheng, One-step approach for constructing high-density single-atom catalysts toward overall water splitting at industrial current densities, Angew. Chem. Int. Ed. (2023), e202214259.
[41] G.Y. Wei, X.P. Liu, Z.W. Zhao, C.B. Men, Y. Ding, S.Y. Gao, Constructing ultrahigh-loading unsymmetrically coordinated Zn-N_3O single-atom sites with efficient oxygen reduction for H_2O_2 production, Chem. Eng. J. 455 (2023), 140721.
[42] Y.H. Xue, Q.H. Yu, Q. Ma, Y.Y. Chen, C.N. Zhang, W. Teng, J.W. Fan, W.X. Zhang, Electrocatalytic hydrogenation boosts reduction of nitrate to ammonia over single-atom Cu with Cu(I)-N_3C_1 Sites, Environ. Sci. Technol. 56 (2022) 14797–14807.
[43] P.P. Li, Z.Y. Jin, Z.W. Fang, G.H. Yu, A single-site iron catalyst with preoccupied active centers that achieves selective ammonia electrosynthesis from nitrate, Energy Environ. Sci. 14 (2021) 3522–3531.
[44] Y. Yao, L. Zhao, J. Dai, J. Wang, C. Fang, G. Zhan, Q. Zheng, W. Hou, L. Zhang, Single atom Ru monolithic electrode for efficient chlorine evolution and nitrate reduction, Angew. Chem. Int. Ed. 61 (2022), E202208215.
[45] Y.Z. Zhang, X. Chen, W.L. Wang, L.F. Yin, J.C. Crittenden, Electrocatalytic nitrate reduction to ammonia on defective Au_1Cu (111) single-atom alloys, Appl. Catal. B Environ. 310 (2022), 121346.
[46] J. Li, Y. Zhang, C. Liu, L. Zheng, E. Petit, K. Qi, Y. Zhang, H. Wu, W. Wang, A. Tiberj, X. Wang, M. Chhowalla, L. Lajaunie, R. Yu, D. Voiry, 3.4% solar-to-ammonia efficiency from nitrate using Fe single atomic catalyst supported on MoS_2 nanosheets, Adv. Funct. Mater. 32 (2021), 2108316.
[47] J. Zhao, X. Ren, X. Liu, X. Kuang, H. Wang, C. Zhang, Q. Wei, D. Wu, Zn single atom on N-doped carbon: highly active and selective catalyst for electrochemical reduction of nitrate to ammonia, Chem. Eng. J. 452 (2023), 139533.
[48] J.M. Cai, Y.Y. Wei, Ang Cao, J.J. Huang, Z. Jiang, S.Y. Lu, S.Q. Zang, Electrocatalytic nitrate-to-ammonia conversion with ~100% Faradaic efficiency via single-atom alloying, Appl. Catal. B Environ. 316 (2022), 121683.
[49] X.Y. Cheng, Z. Shen, L. Jiao, L.J. Yang, X.Z. Wang, Q. Wu, Z. Hu, Tuning metal catalysts via nitrogen-doped nanocarbons for energy chemistry: from metal nanoparticles to single metal sites, EnergyChem 3 (2021), 100066.
[50] H.M. Zhang, W.H. Liu, D. Cao, D.J. Cheng, Carbon-based material-supported single-atom catalysts for energy conversion, iScience 25 (2022), 104367.
[51] Y. Yang, Z. Hu, Y.J. Tian, Y.N. Lu, X.Z. Wang, Y. Chen, High-yield production of quasi-aligned carbon nanotubes by catalytic decomposition of benzene, Nanotechnology 14 (2003) 733–737.
[52] H. Chen, Y. Yang, Z. Hu, K. Huo, Y. Ma, Y. Chen, X. Wang, Y. Lu, Synergism of C_5N six-membered ring and vapor−liquid−solid growth of CN_x nanotubes with pyridine precursor, J. Phys. Chem. B 110 (2006) 16422–16427.
[53] Y. Wang, A. Xu, Z. Wang, L. Huang, J. Li, F. Li, J. Wicks, M. Luo, D.H. Nam, C. S. Tan, Y. Ding, J. Wu, Y. Lum, C.T. Dinh, D. Sinton, G. Zheng, E.H. Sargent, Enhanced nitrate-to-ammonia activity on copper–nickel alloys via tuning of intermediate adsorption, J. Am. Chem. Soc. 142 (2020) 5702–5708.
[54] J. Zhao, Z. Shen, J. Yu, Y. Guo, M.A. Mushtaq, Y. Ding, Z. Song, W. Zhang, X. Huang, Y. Li, D. Liu, X. Cai, Constructing Cu-CuO heterostructured skin on Cu cubes to promote electrocatalytic ammonia production from nitrate wastewater, J. Hazard. Mater. 439 (2022), 129653.
[55] S.W. Han, Y. Kim, K. Kim, Dodecanethiol-derivatized Au/Ag bimetallic nanoparticles: TEM, UV/VIS, XPS, and FTIR analysis, J. Colloid Interface Sci. 208 (1998) 272–278.
[56] J. Yang, H. Qi, A. Li, X. Liu, X. Yang, S. Zhang, Q. Zhao, Q. Jiang, Y. Su, L. Zhang, J. F. Li, Z.Q. Tian, W. Liu, A. Wang, T. Zhang, Potential-driven restructuring of Cu single atoms to nanoparticles for boosting the electrochemical reduction of nitrate to ammonia, J. Am. Chem. Soc. 144 (2022) 12062–12071.
[57] H. Chen, C. Zhang, L. Sheng, M. Wang, W. Fu, S. Gao, Z. Zhang, S. Chen, R. Si, L. Wang, B. Yang, Copper single-atom catalyst as a high-performance electrocatalyst for nitrate-ammonium conversion, J. Hazard. Mater. 434 (2022), 128892.
[58] W.D. Zhang, H.L. Dong, L. Zhou, H.W. Xu, H.R. Wang, X.D. Yan, Y.Q. Jiang, J. W. Zhang, Z.G. Gu, Fe single-atom catalysts with pre-organized coordination structure for efficient electrochemical nitrate reduction to ammonia, Appl. Catal. B Environ. 317 (2022), 121750.
[59] E. Murphy, Y.C. Liu, I. Matanovic, S.Y. Guo, P. Tieu, Y. Huang, A. Ly, S. Das, I. Zenyuk, X.Q. Pan, E. Spoerke, P. Atanassov, Highly durable and selective Fe- and Mo-based atomically dispersed electrocatalysts for nitrate reduction to ammonia via distinct and synergized NO_2^- pathways, ACS Catal. 12 (2022) 6651–6662.
[60] W.J. Bian, X.H. Song, J.W. Shi, X.L. Yin, Nitrogen fixed into HNO_3 by pulsed high voltage discharge, J. Electrostat. 70 (2012) 317–326.
[61] W. Zheng, L. Zhu, Z. Yan, Z. Lin, Z. Lei, Y. Zhang, H. Xu, Z. Dang, C. Wei, C. Feng, Self-activated Ni cathode for electrocatalytic nitrate reduction to ammonia: from fundamentals to scale-up for treatment of industrial wastewater, Environ. Sci. Technol. 55 (2021) 13231–13243.
[62] N.C. Kani, J.A. Gauthier, A. Prajapati, J. Edgington, I. Bordawekar, W. Shields, M. Shields, L.C. Seitz, A.R. Singh, M.R. Singh, Solar-driven electrochemical synthesis of ammonia using nitrate with 11% solar-to-fuel efficiency at ambient conditions, Energy Environ. Sci. 14 (2021) 6349–6359.
[63] K. Han, J.J. Luo, Y.W. Feng, L. Xu, W. Tang, Z.L. Wang, Self-powered electrocatalytic ammonia synthesis directly from air as driven by dual triboelectric nanogenerators, Energy Environ. Sci. 13 (2020) 2450–2458.